AGU PUBLICATIONS

JGR

Journal of Geophysical Research: Space Physics

RESEARCH ARTICLE
10.1002/2015JA021157

Key Points:
- Low O^+/H^+ ratio produced stronger ring current
- Inclusion of physics-based ionospheric outflow leads to a reduction in the CPCP
- Oxygen presence is linked to a nightside reconnection point closer to the Earth

Correspondence to:
R. Ilie,
rilie@umich.edu

Citation:
Ilie, R., M. W. Liemohn, G. Toth, N. Y. Ganushkina, and L. K. S. Daldorff (2015), Assessing the role of oxygen on ring current formation and evolution through numerical experiments, *J. Geophys. Res. Space Physics*, *120*, 4656–4668, doi:10.1002/2015JA021157.

Received 24 FEB 2015
Accepted 17 MAY 2015
Accepted article online 26 MAY 2015
Published online 16 JUN 2015

Assessing the role of oxygen on ring current formation and evolution through numerical experiments

R. Ilie[1], M. W. Liemohn[1], G. Toth[1], N. Yu Ganushkina[1,2], and L. K. S. Daldorff[1]

[1]Atmospheric, Oceanic and Space Sciences, University of Michigan, Ann Arbor, Michigan, USA, [2]Earth Observations, Finnish Meteorological Institute, Helsinki, Finland

Abstract We address the effect of ionospheric outflow and magnetospheric ion composition on the physical processes that control the development of the 5 August 2011 magnetic storm. Simulations with the Space Weather Modeling Framework are used to investigate the global dynamics and energization of ions throughout the magnetosphere during storm time, with a focus on the formation and evolution of the ring current. Simulations involving multifluid (with variable H^+/O^+ ratio in the inner magnetosphere) and single-fluid (with constant H^+/O^+ ratio in the inner magnetosphere) MHD for the global magnetosphere with inner boundary conditions set either by specifying a constant ion density or by physics-based calculations of the ion fluxes reveal that dynamical changes of the ion composition in the inner magnetosphere alter the total energy density of the magnetosphere, leading to variations in the magnetic field as well as particle drifts throughout the simulated domain. A low oxygen to hydrogen ratio and outflow resulting from a constant ion density boundary produced the most disturbed magnetosphere, leading to a stronger ring current but misses the timing of the storm development. Conversely, including a physics-based solution for the ionospheric outflow to the magnetosphere system leads to a reduction in the cross-polar cap potential (CPCP). The increased presence of oxygen in the inner magnetosphere affects the global magnetospheric structure and dynamics and brings the nightside reconnection point closer to the Earth. The combination of reduced CPCP together with the formation of the reconnection line closer to the Earth yields less adiabatic heating in the magnetotail and reduces the amount of energetic plasma that has access to the inner magnetosphere.

1. Introduction

The impact of the polar wind outflow on the evolution of the magnetosphere-ionosphere system was first suggested by *Shelley et al.* [1972]. The abundance of O^+ making up the ring current population was reported by *Hamilton et al.* [1988] based on particle measurements from CHarge Energy Mass spectrometer (CHEM) instrument on the Active Magnetospheric Particle Tracer Explorers/CCE spacecraft, although evidence of its presence throughout the magnetosphere was also provided by several other studies [e.g., *Candidi et al.*, 1982, 1984; *Seki et al.*, 1998; *Mukai et al.*, 1994; *Daglis et al.*, 1999; *Nosé et al.*, 2005]. Large fluxes of oxygen ions streaming with parallel velocities of $v_{||} \sim 10$ km/s have also been reported in the 4–5 R_E polar magnetosphere by several authors [*Waite et al.*, 1985; *Chen et al.*, 1990; *Horwitz et al.*, 1992].

In recent years global modeling studies have shown the possibility that heavy ions of ionospheric origin, in particular oxygen (O^+), could serve as major contributors to the ring current population [*Cladis*, 1986; *Winglee et al.*, 2002; *Glocer et al.*, 2009a; *Garcia et al.*, 2010; *Ilie et al.*, 2013a]. The ionosphere has started to be viewed as a major, often dominant source of magnetospheric plasma and dynamics, in conjunction with the solar wind. The inferred magnitude of the ionospheric outflows was sufficiently large that *Chappell et al.* [1987] and *Huddleston et al.* [2005] suggested that ionospheric ions could be the dominant ion population in the plasma sheet and could entirely control its dynamics. The ambipolar outflow of thermal plasma from the high-latitude ionosphere, made up mainly of H^+, He^+, and O^+ ions and electrons, has a distinct role in determining the global magnetosphere dynamics as well as the plasma transport through the ionosphere-magnetosphere system [*Winglee et al.*, 2002].

The distribution of mass transfer from the ionosphere to the magnetosphere is modulated by both the interplanetary magnetic field and the convection electric fields [e.g., *Howarth and Yau*, 2008]. The reconnection rate is also affected by the presence of heavy ions [e.g., *Shay and Swisdak*, 2004]; therefore, during a substorm with high O^+ abundance, the reconnection rate normalized to the upstream proton Alfven speed is reduced.

Based on Akebono observations, *Cully et al.* [2003a] suggests that the polar wind outflow is strongly correlated with the solar wind density while anticorrelated with the solar wind velocity. The outflow rates of H^+ and O^+ show strong correlation with the solar wind electric field and dynamic pressure while the interplanetary magnetic field (IMF) clock angle does not show any influence on the outflow rate.

When ionospheric plasma is included in simulations, most MHD models seem to show improved agreement with *Dst* observations along with changes in the cross-polar cap potential (CPCP) and alterations of the length of the magnetotail. Ionospheric oxygen outflow from the nightside auroral zone plays a key role in determining plasma sheet density, size, and pressure [*Winglee et al.*, 2002; *Garcia et al.*, 2010; *Wiltberger et al.*, 2010]. The presence of oxygen slows down the convection, decreasing the transpolar potential while altering the density and thermal pressure in the plasma sheet [*Welling et al.*, 2011]. These heavy ions influence the plasma pressure and, therefore, affect the local dynamics. Compositional changes in the inner magnetosphere affect the ring current decay, due to the energy and mass dependence of the charge exchange cross sections [*Ilie et al.*, 2013a, 2013b]. *Glocer et al.* [2009a] shows that by including ionospheric outflow during geomagnetic storms, in addition to a stronger decrease in *Dst* and in the cross-polar cap potential, the root-mean-square error in the simulated magnetic field as compared with various GOES satellites improves by as much as 50%.

During times of strong convection, the increased dayside cold plasma density has been linked to the enhancement of dayside ionospheric outflow. Ions of ionospheric origin are thought to preferentially populate the region where substorm activity occurs and a reduction of convection would reduce the access of the ionospheric ions to this region [*Cully et al.*, 2003b]. Moreover, the composition in the inner magnetosphere changes on a short time scale and over the course of small changes in the IMF, from a magnetosphere dominated by ionosphere plasma to one of solar wind origin [*Winglee et al.*, 2008]. The polar outflow presents short time and spatial-scale fluctuations even during periods of low geomagnetic activity [*Peterson et al.*, 2002]. Moreover, ionospheric outflow could possibly be responsible for the generation of sawtooth oscillations [*Brambles et al.*, 2011, 2013].

Previous studies have only used, at most, two model configurations (e.g., with or without outflow, or two types of outflow, or two magnetospheric model configurations). What has not been done yet is a larger-scale study with several outflow options and several magnetospheric model configurations. This study addresses this issue with a systematic study combining various regional models to explore the influence of model choice on the resulting development of a magnetic storm. Specifically, we will examine simulation results of the global magnetosphere using the Space Weather Modeling Framework (SWMF) to reveal the relative importance of ionospheric outflow and inner magnetospheric composition in the development and evolution of a magnetic storm. The model setup is described in section 2. The results of our study are described in section 3, while section 5 presents a summary of the main findings.

2. Model Specifications

The simulations presented here involve up to four components of the Space Weather Modeling Framework (SWMF) [*Tóth et al.*, 2005, 2012] in various configurations in order to test the relative importance of ionospheric outflow and the ion composition in the inner magnetosphere and on the overall dynamics that control the development of a magnetic storm. The physical domains included in the simulations are the Global Magnetosphere (GM), Ionosphere Electrodynamics (IE), Inner Magnetosphere (IM), and Polar Wind (PW).

2.1. Global Magnetosphere

The GM domain is represented by the Block Adaptive Tree Solar-wind-type Roe Upwind Scheme (BATS-R-US) global magnetohydrodynamic (MHD) model [*Powell et al.*, 1999; *Tóth et al.*, 2006] that solves for the transfer of mass and energy from the solar wind to the magnetosphere. In the simulations described here, BATS-R-US is configured to solve the three-dimensional single-fluid and multifluid MHD equations [*Glocer et al.*, 2009b; *Tóth et al.*, 2012]. This component provides the inner magnetosphere model, the field line volume in the whole IM domain, plasma density, and temperature at the outer boundary of the inner magnetosphere domain as well as the field-aligned currents strength and location for the ionosphere electrodynamics model.

2.2. Inner Magnetosphere

The Rice Convection Model (RCM) [*Harel et al.*, 1981; *Toffoletto et al.*, 2003; *De Zeeuw et al.*, 2004] (the IM model used for this study) calculates the dynamic behavior of the inner magnetospheric particles in the near-Earth region in the spatial domain bounded by closed magnetic field lines and populated by keV energy electrons,

protons, and oxygen ions. The IM component provides the density and pressure along the magnetic field lines and feeds this information to the GM component so that the MHD results are corrected toward the IM results [*De Zeeuw et al.*, 2004], while BATS-R-US sets the RCM outer boundary at the last closed magnetic field boundary calculated by the MHD model. When the RCM is coupled to the single-fluid MHD model (Run 3 and Run 4), in order to define the temperature of the H^+ and O^+ ions in the RCM model, we use the BATS-R-US (MHD) temperature values of the plasma sheet. That is, we calculate $kT = \frac{Pm_p}{\rho}$, where m_p is the proton mass, P is the MHD pressure, and ρ is the MHD density. Therefore, the temperature for the hydrogen and oxygen ions in the RCM code is set to be $\left(\frac{7.8}{8.8}\right) kT$, and the electron temperature is $\left(\frac{1}{8.8}\right) kT$. When the RCM code is coupled with the multifluid MHD model (Run 1 and Run 2), the temperature for both hydrogen and oxygen ions is set by the multifluid MHD model.

2.3. Ionospheric Electrodynamics

The ionospheric electrodynamics (IE) model of *Ridley and Liemohn* [2002] and *Ridley et al.* [2004] consists of an electric potential solver and a model of the electron precipitation to calculate the height-integrated ionospheric quantities at an altitude of ~110 km. Calculations of the conductance pattern and particle precipitation are based on the field-aligned current information passed from the GM component, while the electric potential is passed both to the IM and converted to velocity at the inner boundary of GM.

2.4. Polar Wind Outflow

The ionospheric outflow of electrons and O^+, He^+, and H^+ ions is described by the Polar Wind Outflow Model (PWOM) [*Glocer et al.*, 2007, 2009a], based on the gyrotropic transport equations solved along a number of magnetic field lines [*Gombosi and Nagy*, 1989]. The spatial domain is covering the gap region which spans from ~1000 km in the ionosphere to the inner boundary of the magnetospheric model at 2.5 R_E. The calculated outflow flux sets the inner boundary conditions for the MHD model [*Glocer et al.*, 2009a]. The Mass Spectrometer Incoherent Scatter (MSIS) empirical model provides the neutral densities that are used to calculate chemical losses and sources. In the simulations that do not use PWOM, the MHD inner boundary is set with a passive source term in which the density is kept at a constant value and the radial velocity is set to zero. When an appropriate density is applied, this boundary condition yields a physically reasonable outflow flux to the magnetosphere [*Welling and Liemohn*, 2014].

2.5. Simulation Setup

The coupling between these models is done self-consistently through couplers inside the SWMF. Each of the models within SWMF has been extensively tested, validated, and used for scientific studies of the geospace [*Tóth et al.*, 2005, 2007; *Zhang et al.*, 2007; *Yu and Ridley*, 2009; *Ganushkina et al.*, 2010; *Ilie et al.*, 2010a, 2010b]. An illustration of the components and their coupling within the SWMF is presented in Figure 1.

We conducted four simulations of the 5 August 2011 geomagnetic storm, and Table 1 summarizes the configurations and the details of each run. Run 1 and Run 2 use the multifluid MHD version of the BATS-R-US model, which solves for the continuity, momentum, and energy equation for each species. Run 3 and Run 4 use the single-fluid BATS-R-US model. The composition in the inner magnetosphere was self-consistently solved for Run 1 and Run 2 while for Run 3 and Run 4 it was set to a constant ratio throughout the simulation. The GM inner boundary was set at 2.5 Earth radii (R_E) for all four runs while the inner boundary conditions were set either by the Polar Wind Outflow Model (PWOM) (Run 1) or by a constant density value at the inner boundary of 28 cm^{-3} (Run 2 to Run 4 as described in Table 1). The electric potential is provided by the Ridley Ionospheric Model (RIM) for all runs.

For each of the simulations, GM has a Cartesian grid and the computational domain extends from 32 R_E upstream to 224 R_E downtail, 128 R_E in both y and z directions, adding up to over 2.5 million cells. The grid resolution varies from 1/8 R_E in the spherical shell 2.5 to 3.5 R_E close to the body, to 8 R_E near the outer edges of the domain.

In the case of set constant density on the inner boundary, the numerical diffusion is controlling the outflow rate. However, numerical diffusion is proportional with the grid size, and in this study we use relatively high resolution, especially near the inner boundary. In addition, we employ the Boris correction [*Boris*, 1970] which artificially reduces the speed of light, allowing the Alfven speed to be limited to the speed of light, and so we can use a method to increase the time step. Because numerical diffusion is dependent on the maximum wave speed in the simulation [*Powell et al.*, 1999], using the Boris correction also inhibits the numerical diffusion. Therefore, even though the outflow is driven initially by the (reduced) numerical diffusion, the MHD regime

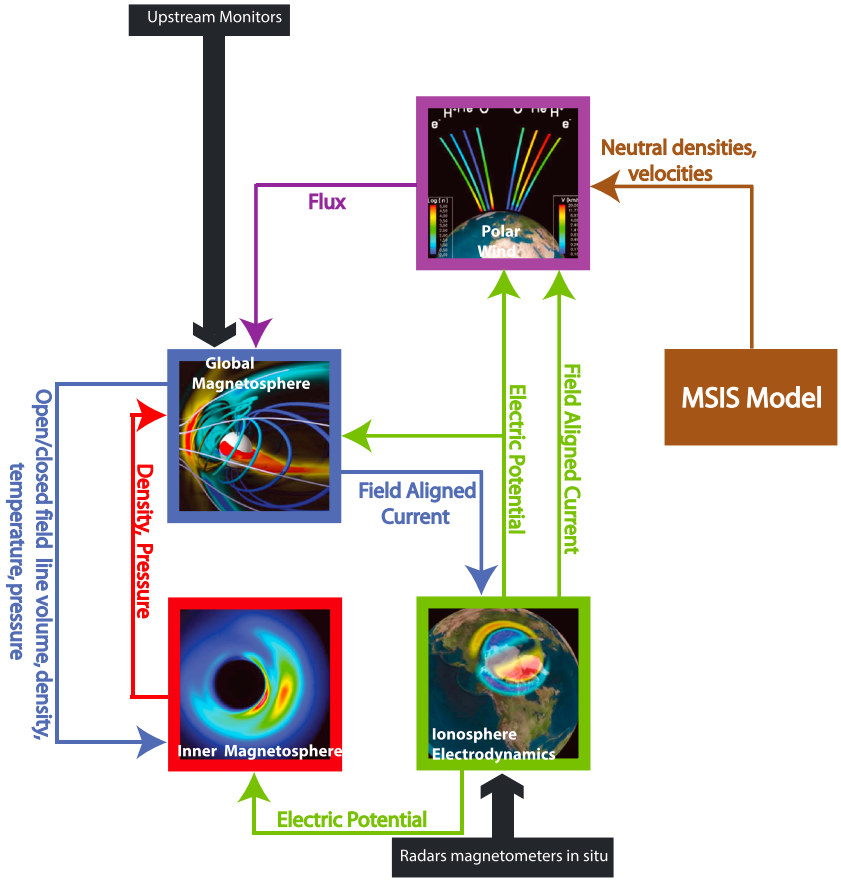

Figure 1. Coupling schematic of the model couplings within SWMF.

overcompensates fast enough to accelerate the particles into geospace. For more details, see *Welling and Liemohn* [2014].

All simulations were first ran to reach steady state for the first 2500 iterations with independent local time stepping within each cell of the BATS-R-US grid. This means that each cell uses a time step based on the local numerical stability criteria, allowing the BATS-R-US model to accelerate the convergence toward a steady state. After the steady state is reached, the simulation was allowed to run in the time accurate mode. The coupling frequency of GM with IM, IE, and PW is 10 s while GM and IE exchange information every 5 s. Also, the IM-IE and PW-IE coupling frequency was of 10 s.

Table 1. Simulation Setups

Component	Run 1	Run 2	Run 3	Run 4
GM	Multifluid BATS-R-US	Multifluid BATS-R-US	Single-fluid BATS-R-US	Single-fluid BATS-R-US
IM	RCM with composition from GM	RCM with composition from GM	RCM with 90% H and 10% O	RCM with 70% H and 30% O
IE	RIM	RIM	RIM	RIM
PW	PWOM	Inner BC: $r = 2.5$ $n_{H^+} = 28\ cm^{-3}$, $n_{O^+} = 2.8\ cm^{-3}$	Inner BC: $r = 2.5$ $n = 28\ cm^{-3}$	Inner BC: $r = 2.5$ $n = 28\ cm^{-3}$

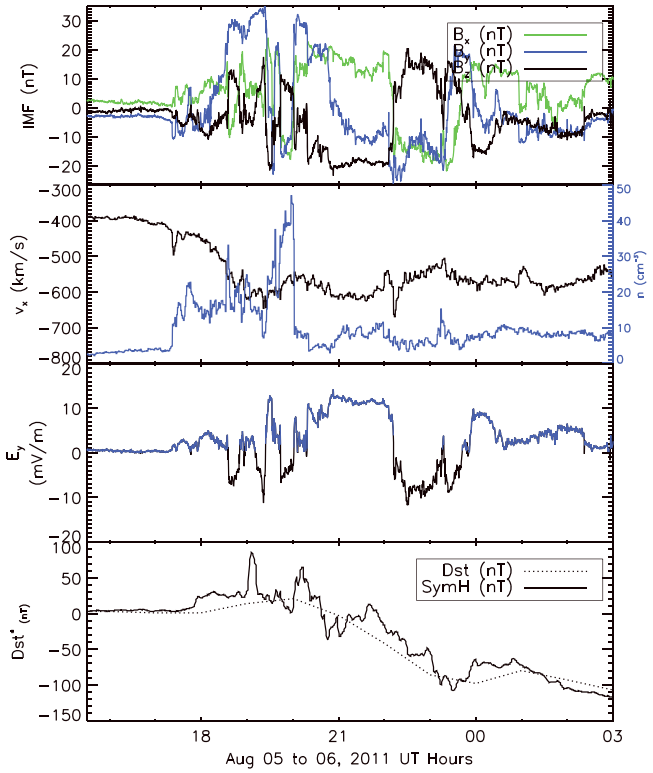

Figure 2. 5 August 2011 event parameters. (first panel to fourth panel) We present all components of the interplanetary magnetic field (B_x green line, B_y blue line, and B_z black line) followed the earthward component of the solar wind velocity (black line) and number density (blue line). Figure 2 (third panel) shows the eastward component of the interplanetary electric field (blue/black indicates positive/negative values). Figure 2 (fourth panel) shows the *Dst* and *Sym-H* indices (dotted and solid black lines).

Since we do not attempt to reproduce the high level of turbulent transport usually observed in the magnetospheric plasma [e.g., *Wang et al.*, 2010; *Stepanova et al.*, 2011], this simulation setup is ideal for describing the global average state of the near-Earth environment system.

3. Results

3.1. The 5 August 2011 Geomagnetic Storm

The active sunspot region 1261 flared early on 4 August, and the coronal mass ejection (CME) from this flare eventually led to a geomagnetic storm the next day that produced a steep decrease in the *Dst* index to −113 nT while the *Sym-H* index reached a minimum of −126 nT. This is one of the largest CME-driven storms that occurred at the end of the prolonged solar minimum leading into solar cycle 24. Figure 2 shows the three components of the interplanetary magnetic field (IMF) in GSM coordinates as measured by the ACE spacecraft (first panel) during this event. Figure 2 (second panel) shows the earthward component of the solar wind velocity and solar wind number density. These quantities are also used as input in the SWMF simulation. Figure 2 (third panel) presents the eastward component of the interplanetary electric field while in Figure 2 (fourth panel) the Kyoto *Dst* (1 h resolution) and the *Sym-H* (1 min resolution) geomagnetic indices are presented.

The solar wind conditions for this event are characterized by a region of increased number density that begins at ~1720 UT and doubles relative to its value during the prestorm quiet time period. The solar wind number density continues to increase during the initial phase of the storm, reaching a maximum value of 47 cm^{-3} at ~2000 UT, when it sharply drops to 8 cm^{-3}. This time marks the beginning of the storm main phase when the IMF turns southward, reaching the largest negative value of ~−20 nT at ~1930 UT; it stays negative for the following 2.5 h and turns northward for another 2 h. The earthward solar wind velocity starts to increase from 400 km/s to about 600 km/s and remains elevated throughout the storm. The storm recovery lasted several days.

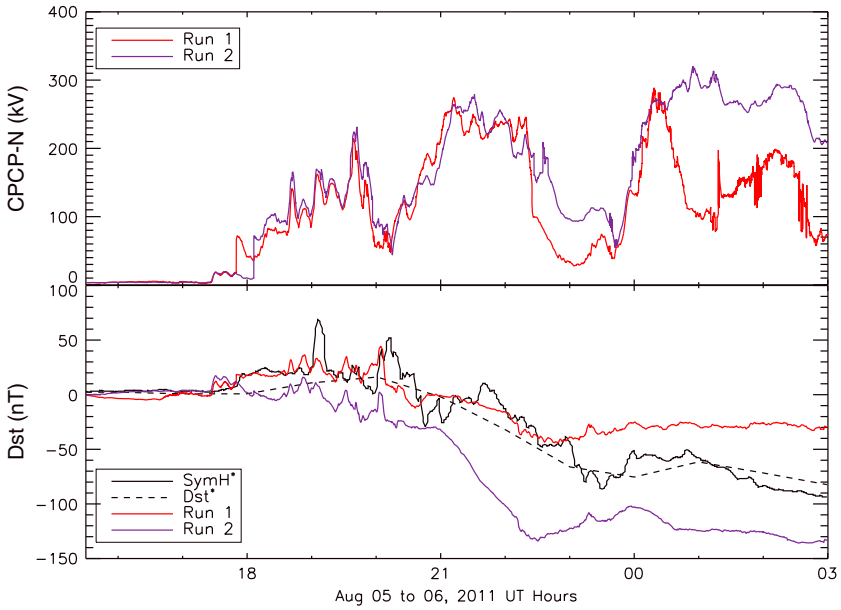

Figure 3. (top) Simulation results for the cross-polar cap potential in the Northern Hemisphere (CPCP-N) for Run 1 (red line) and Run 2 (magenta line) are presented. (bottom) The simulated *Sym-H* indices for the two runs (color coded as above) along with the observationally based indices *Dst** (dashed back line) and *Sym-H** (solid black line).

3.2. Polar Outflow Effects

Figure 3 presents the simulation results from Run 1 and Run 2, comparing the influence of the physics-based polar outflow at the inner boundary as opposed to the outflow produced by a prescribed constant density at the inner boundary.

Figure 3 (top) presents the simulated cross-polar cap potential in the Northern Hemisphere from Run 1 (red line) and Run 2 (purple line). Figure 3 (bottom) shows the *Dst** and *Sym-H** indices (dashed and solid black lines, respectively) along with the synthetically produced *Sym-H* index from the two simulations. The lines are color coded as in the panel above.

The synthetic *Sym-H* index is calculated with the Biot-Savart integral for all the electric currents encompassed by the BATS-R-US simulation domain from the inner boundary outward. This quantity is used as a proxy for the magnetosphere response to the geomagnetic disturbance as calculated by the model. As this synthetic index is not directly comparable with *Dst* and *Sym-H*, the two observationally based indices (*Dst* and *Sym-H*) also cannot be directly compared due to different methodologies used to obtain them (see the study by *Katus and Liemohn*, 2013 [2013]). However, they carry important information regarding the response of the magnetosphere to the incoming solar wind.

Since the SWMF calculated synthetic *Sym-H* values include contributions from all currents except the effects of the induced currents within the Earth, the *Dst** and *Sym-H** indices are only corrected to exclude the contribution from the induced currents in the Earth. Therefore, $Sym\text{-}H^* = Sym\text{-}H/C_{IC}$ and $Dst^* = Dst/C_{IC}$, where $C_{IC} = 1.3$ [*Dessler and Parker*, 1959; *Langel and Estes*, 1985; *Kozyra and Liemohn*, 2003]. Due to its much higher time resolution, *Sym-H** allows for a better comparison with computed output.

The results of Run 2 indicate that not only a stronger magnetic storm is developing but also the magnetosphere responds faster than the observations suggest. The synthetic *Sym-H* produced by Run 1 seems to have the same timing as the observed *Sym-H**, as reflected by the high correlation coefficient between the model result and the observationally based indices (0.82 correlation with *Dst** and 0.85 correlation coefficient for *Sym-H**; please note that *Dst** versus *Sym-H** have a correlation coefficient of 0.85 as well).

Even though Run 1 fails to produce a significant disturbance in the geomagnetic field, with the minimum simulated *Sym-H* reaching only −44 nT, the high correlation coefficient between the simulated and observed indices suggests that the simulation setup from Run 1 produces a reasonable response of the magnetosphere to the solar wind conditions and it is closer to *Dst* observations during storm main phase. Since we

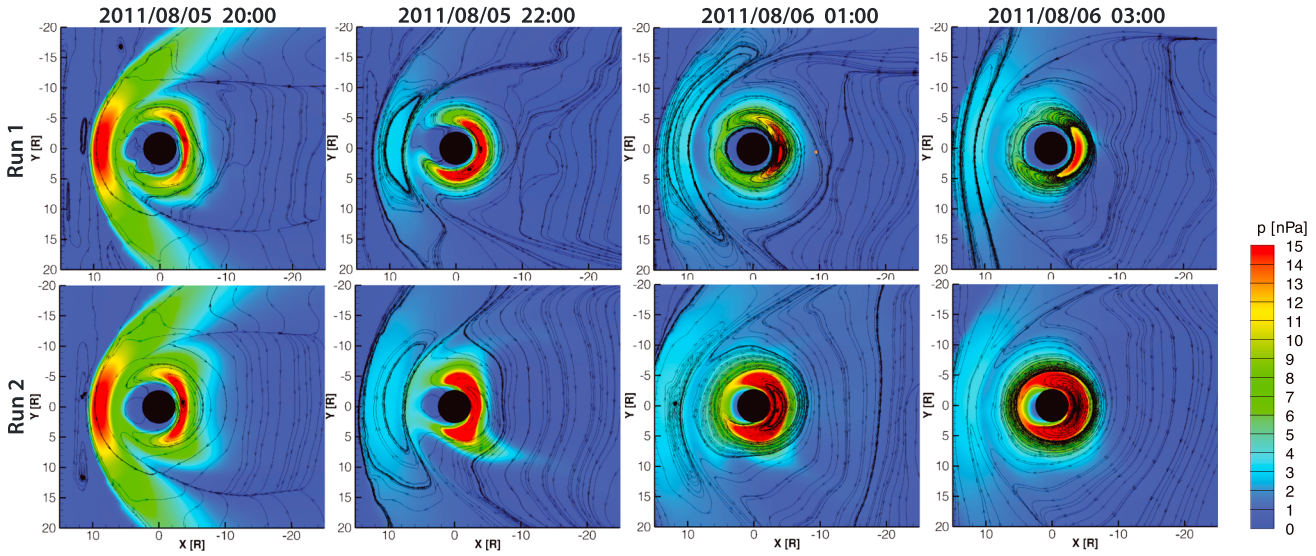

Figure 4. Pressure (color contours) and current projections (streamlines) in the $z = 0$ plane from (top row) Run 1 and (bottom row) Run 2 at four distinct times during the simulations.

are interested more in the overall response of the magnetosphere to the solar wind conditions than one to one absolute matching of observations, based on analysis of the correlation coefficients, the multifluid MHD coupled with the polar wind outflow produces a reasonable agreement between the model and observations during the 5 August 2011 magnetic storm.

The simulated cross-polar cap potentials are very similar for the two runs, up to ~2400 UT on 5 August. During the second long-lasting southward turning of the IMF B_z, the CPCP produced by Run 1 also shows an increase correlated with the southward turning of the IMF B_z. Conversely, the CPCP produced by Run 2 shows no change and remains elevated throughout the recovery phase. However, despite the strong convection during the main phase of the storm, the ring current does not intensify but rather shows signs of recovery. This might be due to the fact that even though the convection is high during this time, the low pressure (see Figure 4) in the inner magnetosphere (indicative of low plasma sheet number density) is followed by the flushing of high-density plasma from the inner magnetosphere, leading to a rapid loss of ring current ions. This finding is also consistent with *Liemohn and Kozyra* [2005].

Figure 4 presents the color contours of the pressure and streamlines of the current projections in the $z = 0$ plane from Run 1 and Run 2. In the case of physics-based outflow (Run 1), the pressure in the inner magnetosphere is much smaller compared to the case of Run 2, leading to a weaker and spatially constrained ring current.

The simulation results for the magnitude of the eastward component of the electric field (color contours) and the stream traces indicate the projections of the magnetic field lines on the $y = 0$ plane are presented in Figure 5. For comparison purposes, we limited the box size to X:[−20 R_E, 15 R_E] and Z:[−20 R_E, 20 R_E] in the plot for all time snapshots during the storm evolution. One striking feature is that the results of Run 2 shows a nightside reconnection line that is farther from Earth, while the inclusion of the Polar Wind Outflow Model in the run setup (Run 1) produces an X line closer to the planet. This is especially easily seen for 2200, 2200, and 0100UT, when the reconnection line for Run 1 resides inside the plotting box, while for Run 2 is further than 20 R_E down the tail. Run 2 produces an inflated magnetosphere, pushing the nightside reconnection line far in the tail; therefore, a more distant neutral line allows for more adiabatic heating leading to a stronger intensification of the ring current.

3.3. Composition Effects

Run 3 and Run 4 were set up to use a constant ratio of hydrogen to oxygen ions to be fed into the inner magnetosphere model (RCM). Therefore, the only difference between the two runs is that Run 4 assumes a 7 to 3 ratio of hydrogen to oxygen ions as opposed to 9 to 1 for Run 3 (in terms of number density). Figure 6 (top) presents the simulated cross-polar cap potential in the Northern Hemisphere from Run 3 (blue line) and Run 4

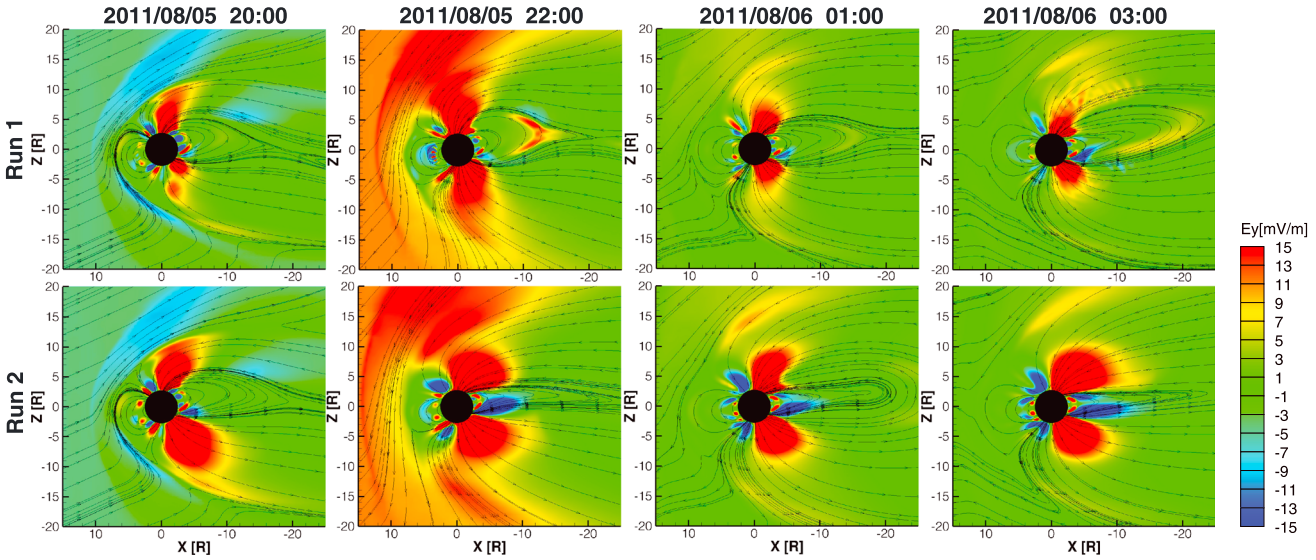

Figure 5. Eastward component of the electric field (color contours) and magnetic field projections (streamlines) in the $y = 0$ plane from (top row) Run 1 and (bottom row) Run 2 at four distinct times during the simulations.

(yellow line). Figure 6 (bottom) shows the *Dst** and *Sym-H** indices (dashed and solid black lines, respectively) along with the synthetically produced *Sym-H* index from the two simulations. The lines are color coded as in the panel above.

For the first 4.5 h of the simulation, the two runs produce similar results. However, after the IMF B_z turns southward (~2000 UT), the simulation results start to significantly diverge. The synthetic *Sym-H* produced by Run 3 starts to drop sooner than the observed *Sym-H* index, and it reached a minimum (−133 nT) lower than that observed. Conversely, the response of the magnetosphere during Run 4 is weaker, producing a simulated minimum *Sym-H* of only −31.5 nT. The cross-polar cap potentials produced by the two runs are similar only until the IMF B_z turns southward and after that the convection in the ionosphere starts to differ between the two runs. Run 4 produces a systematically higher CPCP, except for the time interval when the IMF B_z turns

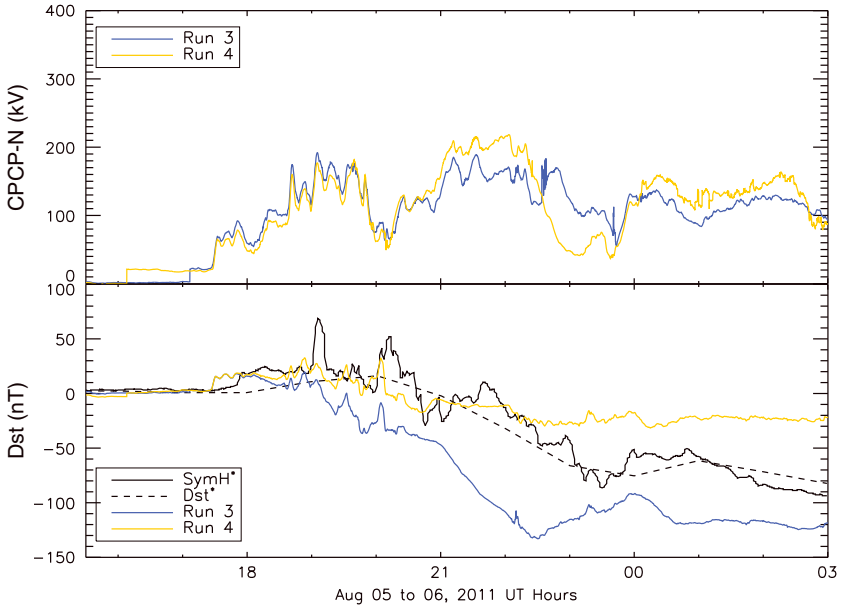

Figure 6. (top) Simulation results for the cross-polar cap potential in the Northern Hemisphere (CPCP-N) for Run 3 (blue line) and Run 4 (yellow line) are presented. (bottom) The simulated *Sym-H* indices for the two runs (color coded as above) along with the observationally based indices *Dst** (dashed back line) and *Sym-H** (solid black line).

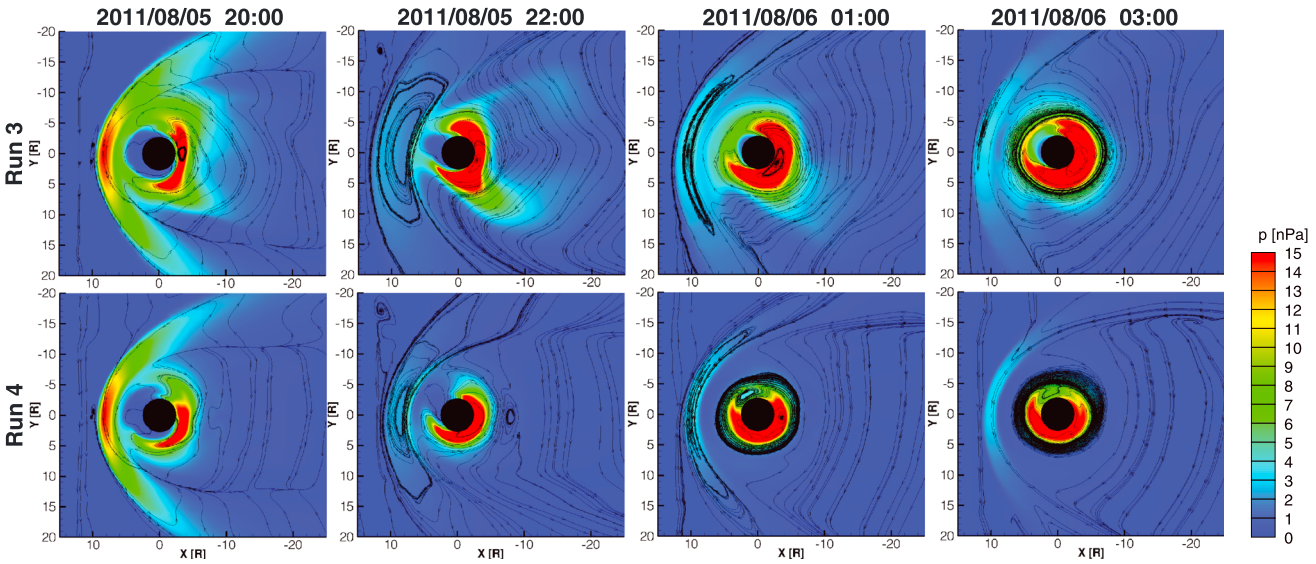

Figure 7. Pressure (color contours) and current projections (streamlines) in the $z = 0$ plane from (top row) Run 3 and (bottom row) Run 4 at four distinct times during the simulations.

northward (2000 UT to 2400 UT). The stronger ring current produced by Run 3 also gives rise to stronger Region-2 currents which act to weaken the low-latitude electric field, hence shielding the inner magnetosphere from the dawn-dusk electric field. This in turn will lower the cross-polar cap potential, as we see in Figure 6.

Figure 7 presents the pressure contours and current projections on the $z = 0$ plane. We note that Run 3 produces an increased pressure in the inner magnetosphere as compared to the results obtained using the simulation setup from Run 4. However, this is to be expected since the ratio on H^+ to O^+ in the inner magnetosphere is set to a constant value, and the mass conservation across the nightside IM boundary allows for a higher particle number density when we assume a larger fraction of protons, therefore leading to an increased plasma pressure in the inner magnetosphere.

Figure 8 shows the model results for the magnitude of the eastward component of the electric field (color contours) while the stream traces indicate the magnetic field lines. We note that for the case when hydrogen is the more dominant ion in the inner magnetosphere simulation (Run 3), the *y* component of the electric field is much weaker in the polar region, consistent with the reduced cross-polar cap potential (see Figure 6).

The increased inner magnetospheric pressure in the Run 3 results inflates the magnetosphere while pushing the nightside neutral line farther from the body. These findings are also consistent with *De Zeeuw et al.* [2004]. The protruded magnetosphere allows the solar wind to be diverted around the magnetosphere rather than piling-up, reducing the amount of magnetic reconnection that takes place at the magnetopause. Hence, the convection together with the cross-polar cap potential are reduced.

The location of the nightside neutral X line has great importance in determining the amount of adiabatic heating that occurs; therefore, the closer the nightside reconnection line gets to the Earth, the less adiabatic heating takes place. This in turn reduces the amount of heated plasma that has access to the inner magnetosphere, resulting in a weaker ring current, leading to the development of a less intense storm (Run 4).

Both Run 1 and Run 4 predict weaker ring current due to the neutral line location being closer to the Earth in these simulations. One similarity of those 2 runs is that higher percentages of oxygen populate the magnetosphere. We can infer from this that the presence of oxygen in the plasma sheet can affect the global magnetospheric structure and dynamics and brings the neutral line closer to the Earth. However, the eastward component of the electric field is stronger in the case of no PWOM-driven outflow, and this can also be seen in Figure 3.

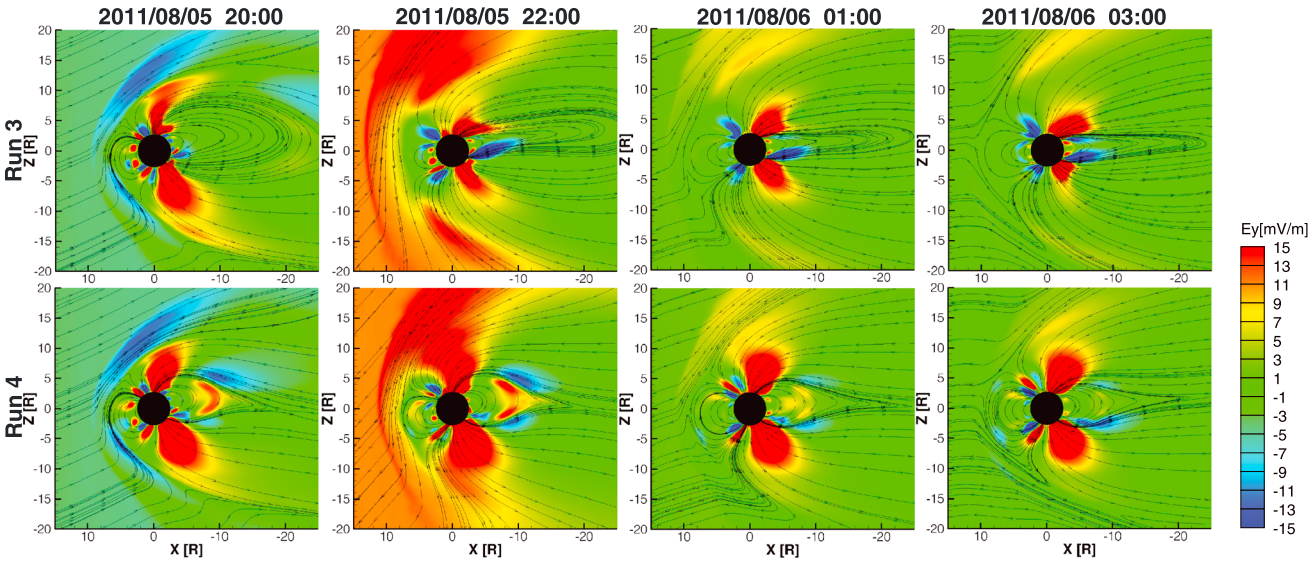

Figure 8. Eastward component of the electric field (color contours) and magnetic field projections (streamlines) in the $y = 0$ plane from (top row) Run 3 and (bottom row) Run 4 at four distinct times during the simulations.

4. Discussion

A summary of our findings is presented in Table 2. We found that the simulations that allowed for a low oxygen to hydrogen ratio and constant outflow produced the most disturbed magnetosphere leading to a stronger ring current, in agreement with the findings of *Glocer et al.* [2013]. This is mainly due to the fact that the magnetospheric composition in the constant outflow run is dominated by hydrogen (not shown here) and higher number density plasma. However, the synthetic *Sym-H* drops too quickly and too sharp, which leads us to believe that the constant ion flux in the inner boundary of the MHD code misses the timing of the storm development. Inclusion of the physics-based polar outflow model leads to a high correlation coefficient between the modeled *Sym-H* index and its observed counterpart. That is, the synthetic *Sym-H* produced by Run 1 shows similar timing as the observed *Sym-H**, as reflected by the high correlation coefficient between the model result and the observationally based indices (0.82 correlation with *Dst** and 0.85 correlation coefficient for *Sym-H*).

Changing the composition in the inner magnetosphere in a dynamic way alters the total ring current pressure, which acts as a proxy for the total energy density of the magnetosphere, leading to changes in the magnetic field as well as particle trajectories throughout the simulated domain.

Conversely, adding ionospheric outflow to the magnetosphere system leads to a reduction in the transpolar potential, a finding consistent with *Winglee et al.* [2002], *Glocer et al.* [2009a], and *Garcia et al.* [2010].

In this case, it might be due to the fact that near the inner boundary, where the outflow occurs, the increase of mass alters the calculation of the current in this region, which is directly linked to the ionospheric potential. This also changes the particle precipitation which by extension alters the height-integrated conductivity in

Table 2. Summary of Findings[a]

Run 2 Versus Run 1	Run 3 Versus Run 4
farther nightside X line	farther nightside X line
higher equatorial plasma pressure	higher equatorial plasma pressure
stronger storm	stronger storm
higher E_y	lower E_y
higher CPCP during recovery phase	lower CPCP

[a]Less oxygen in the inner magnetosphere will lead to the results mentioned above.

the ionosphere. Also, just as in the case of *Winglee et al.* [2002], the reduction on the transpolar potential is due to the mass loading the magnetosphere which in turn affects the momentum transfer between the solar wind and the magnetosphere. However, the relative contribution of these effects requires additional investigation and is subject to future study.

This changing in the polar cap potential can further alter not only the solution in the magnetosphere but it can provide feedback to the calculated outflow as well. The presence of oxygen in the plasma sheet can affect the global magnetospheric structure and dynamics. Moreover, the nightside reconnection point is brought closer to Earth. The combination of reduced CPCP together with an earthward reconnection line yields less adiabatic heating. This reduces the amount of heated plasma that has access to the inner magnetosphere producing a weaker ring current, therefore a less intense storm. However, the synthetic *Sym-H* is highly correlated with its observed counterparts. If we would infer from the results of the single-fluid runs, the variation of the ionospheric convection potential is not only the primary indication of change in storm strength but is rather linked to the composition, neutral line location, and pressure/density peak in the inner magnetosphere.

The simulations that allowed for enhanced O^+/H^+ ratios (by either including the polar wind outflow or increasing the constant ratio) suggested that increasing the oxygen abundance in the inner magnetosphere will bring the nightside neutral line closer to the Earth. At the same time, the pressure in the inner magnetosphere decreases, leading to a weaker ring current.

5. Summary and Conclusions

We have analyzed the effect of ionospheric outflow and magnetospheric ion composition on the physical processes that control the development of the 5 August 2011 magnetic storm. This event was one of the largest CME-driven storms that occurred at the end of the prolonged solar minimum leading into solar cycle 24 and produced a disturbance in the geomagnetic field larger than 100 nT. Simulations using the SWMF in various setups are used to investigate the global dynamics and energization of ions throughout the magnetosphere, with a focus on the formation and evolution of the ring current during storm time. For this purpose we conducted numerical simulations involving multifluid (with variable H^+/O^+ ratio in the inner magnetosphere) and single-fluid (with constant H^+/O^+ ratio in the inner magnetosphere) MHD for the global magnetosphere. The conditions on the inner boundary were set either by specifying a constant ion density of 28 cm^{-3} or by physics-based calculations of the ion fluxes by the Polar Wind Outflow Model.

We found that changes of the ion composition in the inner magnetosphere alter the total ring current pressure, which acts as a proxy for the energy density of the magnetosphere, leading to variations in the magnetic field. This in turn change the particle drifts throughout the simulated domain.

A low oxygen to hydrogen ratio and outflow resulting from a constant ion density boundary produced the most disturbed magnetosphere leading to a stronger ring current. However, this simulation setup leads to time shift in the storm development. Conversely, including a physics-based solution for the ionospheric outflow (PWOM) to the magnetosphere system leads to a reduction in the cross-polar cap potential.

The presence of oxygen in the plasma sheet affects the global magnetospheric structure and dynamics and brings the nightside reconnection point closer to the Earth. The combination of reduced CPCP together with an earthward reconnection line yields less adiabatic heating in the magnetotail and reduces the amount of energetic plasma that has access to the inner magnetosphere.

Acknowledgments

Work at University of Michigan was performed with financial support from NSF grant AGS-1102863 and NASA grant NNX13AG26G and NNX14AC02G. Numerical simulations were performed on NASA Pleiades super computer clusters. The part of the research done by N. Ganushkina leading to these results has received funding from the European Union Seventh Framework Programme (FP7/2007–2013) under grant agreements 606716 SPACESTORM and from the European Union's Horizon 2020 research and innovation programme under grant agreement 637302 PROGRESS. N. Ganushkina's work was also partly funded by the Academy of Finland. R. Ilie and N. Ganushkina thank the International Space Science Institute (ISSI) in Bern, Switzerland, for its support of an International team on "Analysis of Cluster Inner Magnetosphere Campaign data, in application the dynamics of waves and wave-particle interaction within the outer radiation belt." The authors would like to thank the Kyoto World Data Center for the *Dst* index and CDAWeb for allowing access to the plasma and magnetic field data of the Wind and ACE spacecraft. The data resulting from the numerical simulations are available upon request to the authors.

Alan Rodger thanks Elizaveta Antonova and one anonymous reviewer for their assistance in evaluating this paper.

References

Boris, J. P. (1970), A physically motivated solution of the Alfven problem. Internal report at Naval Research Laboratory, NRL Memorandum Rep., Naval Research Laboratory, Washington, D. C.

Brambles, O. J., W. Lotko, B. Zhang, M. Wiltberger, J. Lyon, and R. J. Strangeway (2011), Magnetosphere sawtooth oscillations induced by ionospheric outflow, *Science*, *332*(6), 1183–1186.

Brambles, O. J., W. Lotko, B. Zhang, J. Ouellette, J. Lyon, and M. Wiltberger (2013), The effects of ionospheric outflow on ICME and SIR driven sawtooth events, *J. Geophys. Res. Space Physics*, *118*, 6026–6041, doi:10.1002/jgra.50522.

Candidi, M., S. Orsini, and V. FORMISANO (1982), The properties of ionospheric O^+ ions as observed in the magnetotail boundary-layer and northern plasma lobe, *J. Geophys. Res.*, *87*(NA11), 9097–9106.

Candidi, M., S. Orsini, and A. G. Ghielmetti (1984), Observations of multiple ion beams in the magnetotail: Evidence for a double proton population, *J. Geophys. Res.*, *89*(A4), 2180–2184.

Chappell, C. R., T. E. Moore, and J. H. Waite Jr. (1987), The ionosphere as a fully adequate source of plasma for the Earth's magnetosphere, *J. Geophys. Res.*, *92*, 5896–5910, doi:10.1029/JA092iA06p05896.

Chen, M. W., M. Ashour-Abdalla, W. K. Peterson, T. E. Moore, and A. M. Persoon (1990), Plasma characteristics of upflowing ion beams in the polar cap region, *J. Geophys. Res.*, *95*, 3907–3924, doi:10.1029/JA095iA04p03907.

Cladis, J. B. (1986), Parallel acceleration and transport of ions from polar ionosphere to plasma sheet, *Geophys. Res. Lett.*, *13*(9), 893–896.

Cully, C. M., E. F. Donovan, A. W. Yau, and G. G. Arkos (2003a), Akebono/suprathermal mass spectrometer observations of low-energy ion outflow: Dependence on magnetic activity and solar wind conditions, *J. Geophys. Res.*, *108*(A2), 1093, doi:10.1029/2001JA009200.

Cully, C. M., E. F. Donovan, A. W. Yau, and H. J. Opgenoorth (2003b), Supply of thermal ionospheric ions to the central plasma sheet, *J. Geophys. Res.*, *108*(A2), 1092, doi:10.1029/2002JA009457.

Daglis, I. A., R. M. Thorne, W. Baumjohann, and S. Orsini (1999), The terrestrial ring current: Origin, formation, and decay, *Rev. Geophys.*, *37*, 407–438, doi:10.1029/1999RG900009.

De Zeeuw, D. L., S. Sazykin, R. A. Wolf, T. I. Gombosi, A. J. Ridley, and G. Toth (2004), Coupling of a global MHD code and an inner magnetospheric model: Initial results, *J. Geophys. Res.*, *109*, A12219, doi:10.1029/2003JA010366.

Dessler, A. J., and E. N. Parker (1959), Hydromagnetic theory of geomagnetic storms, *J. Geophys. Res.*, *64*, 2239–2252, doi:10.1029/JZ064i012p02239.

Ganushkina, N. Y., M. W. Liemohn, M. V. Kubyshkina, R. Ilie, and H. J. Singer (2010), Distortions of the magnetic field by storm-time current systems in Earth's magnetosphere, *Ann. Geophys.*, *28*, 123–140, doi:10.5194/angeo-28-123-2010.

Garcia, K. S., V. G. Merkin, and W. J. Hughes (2010), Effects of nightside O^+ outflow on magnetospheric dynamics: Results of multifluid MHD modeling, *J. Geophys. Res.*, *115*, A00J09, doi:10.1029/2010JA015730.

Glocer, A., G. Toth, and T. Gombosi (2007), Modeling ionospheric outflow during a geomagnetic storm, *Eos Trans. AGU*, *88*(52), Fall Meet. Suppl., Abstracts SA51B–0521.

Glocer, A., G. Tóth, T. Gombosi, and D. Welling (2009a), Modeling ionospheric outflows and their impact on the magnetosphere: Initial results, *J. Geophys. Res.*, *114*, A05216, doi:10.1029/2009JA014053.

Glocer, A., G. Tóth, Y. Ma, T. Gombosi, J.-C. Zhang, and L. M. Kistler (2009b), Multifluid Block-Adaptive-Tree Solar wind Roe-type Upwind Scheme: Magnetospheric composition and dynamics during geomagnetic storms: Initial results, *J. Geophys. Res.*, *114*, A12203, doi:10.1029/2009JA014418.

Glocer, A., M. Fok, X. Meng, G. Tóth, N. Buzulukova, S. Chen, and K. Lin (2013), CRCM + BATS-R-US two-way coupling, *J. Geophys. Res. Space Physics*, *118*(4), 1635–1650, doi:10.1002/jgra.50221.

Gombosi, T. I., and A. F. Nagy (1989), Time-dependent modeling of field-aligned current-generated ion transients in the polar wind, *J. Geophys. Res.*, *94*, 359–369, doi:10.1029/JA094iA01p00359.

Hamilton, D. C., G. Gloeckler, F. M. Ipavich, B. Wilken, and W. Stuedemann (1988), Ring current development during the great geomagnetic storm of February 1986, *J. Geophys. Res.*, *93*, 14,343–14,355, doi:10.1029/JA093iA12p14343.

Harel, M., R. A. Wolf, P. H. Reiff, R. W. Spiro, W. J. Burke, F. J. Rich, and M. Smiddy (1981), Quantitative simulation of a magnetospheric substorm. I: Model logic and overview, *J. Geophys. Res.*, *86*, 2217–2241, doi:10.1029/JA086iA04p02217.

Horwitz, J. L., C. J. Pollock, T. E. Moore, W. K. Peterson, J. L. Burch, J. D. Winningham, J. D. Craven, L. A. Frank, and A. Persoon (1992), The polar cap environment of outflowing O(+), *J. Geophys. Res.*, *97*, 8361–8379, doi:10.1029/92JA00147.

Howarth, A., and A. W. Yau (2008), The effects of IMF and convection on thermal ion outflow in magnetosphere-ionosphere coupling, *J. Atmos. Sol. Terr. Phys.*, *70*, 2132–2143, doi:10.1016/j.jastp.2008.08.008.

Huddleston, M. M., C. R. Chappell, D. C. Delcourt, T. E. Moore, B. L. Giles, and M. O. Chandler (2005), An examination of the process and magnitude of ionospheric plasma supply to the magnetosphere, *J. Geophys. Res.*, *110*, A12202, doi:10.1029/2004JA010401.

Ilie, R., M. W. Liemohn, J. Borovsky, and J. Kozyra (2010a), An investigation of the magnetosphere-ionosphere response to real and idealized CIR events through global MHD simulations, *Proc. R. Soc. A*, *466*, 3279–3303, doi:10.1098/rspa.2010.0074.

Ilie, R., M. W. Liemohn, and A. Ridley (2010b), The effect of smoothed solar wind inputs on global modeling results, *J. Geophys. Res.*, *115*, A01213, doi:10.1029/2009JA014443.

Ilie, R., R. M. Skoug, H. O. Funsten, M. W. Liemohn, J. J. Bailey, and M. Gruntman (2013a), The impact of geocoronal density on ring current development, *J. Atmos. Sol. Terr. Phys.*, *99*, 92–103, doi:10.1016/j.jastp.2012.03.010.

Ilie, R., R. M. Skoug, P. Valek, H. O. Funsten, and A. Glocer (2013b), Global view of inner magnetosphere composition during storm time, *J. Geophys. Res. Space Physics*, *118*, 7074–7084, doi:10.1002/2012JA018468.

Katus, R. M., and M. W. Liemohn (2013), Similarities and differences in low- to middle-latitude geomagnetic indices, *J. Geophys. Res. Space Physics*, *118*, 5149–5156, doi:10.1002/jgra.50501.

Kozyra, J. U., and M. W. Liemohn (2003), Ring current energy input and decay, *Space Sci. Rev.*, *109*, 105–131, doi:10.1023/B:SPAC.0000007516.10433.ad.

Langel, R. A., and R. H. Estes (1985), Large-scale, near-field magnetic fields from external sources and the corresponding induced internal field, *J. Geophys. Res.*, *90*, 2487–2494, doi:10.1029/JB090iB03p02487.

Liemohn, M. W., and J. U. Kozyra (2005), Testing the hypothesis that charge exchange can cause a two-phase decay, in *The Inner Magnetosphere: Physics and Modeling, Geophys. Monogr. Ser.*, vol. 155, edited by T. I. Pulkkinen, N. A. Tsyganenko, and R. H. W. Friedel, pp. 211, AGU, Washington, D. C.

Mukai, T., M. Hirahara, S. Machida, Y. Saito, T. Terasawa, and A. Nishida (1994), Geotail observation of cold ion streams in the medium distance magnetotail lobe in the course of a substorm, *Geophys. Res. Lett.*, *21*(11), 1023–1026.

Nosé, M., S. Taguchi, K. Hosokawa, S. P. Christon, R. W. McEntire, T. E. Moore, and M. R. Collier (2005), Overwhelming O^+ contribution to the plasma sheet energy density during the October 2003 superstorm: Geotail/EPIC and IMAGE/LENA observations, *J. Geophys. Res.*, *110*, A09S24, doi:10.1029/2004JA010930.

Peterson, W. K., H. L. Collin, M. Boehm, A. W. Yau, C. Cully, and G. Lu (2002), Investigation into the spatial and temporal coherence of ionospheric outflow on January 9–12, 1997, *J. Atmos. Sol. Terr. Phys.*, *64*, 1659–1666, doi:10.1016/S1364-6826(02)00136-0.

Powell, K. G., P. L. Roe, T. J. Linde, T. I. Gombosi, and D. L. De Zeeuw (1999), A solution-adaptive upwind scheme for ideal magnetohydrodynamics, *J. Comput. Phys.*, *154*, 284–309, doi:10.1006/jcph.1999.6299.

Ridley, A., T. Gombosi, and D. Dezeeuw (2004), Ionospheric control of the magnetosphere: Conductance, *Ann. Geophys.*, *22*, 567–584.

Ridley, A. J., and M. W. Liemohn (2002), A model-derived storm time asymmetric ring current driven electric field description, *J. Geophys. Res.*, *107*(A8), 1151, doi:10.1029/2001JA000051.

Seki, K., T. Terasawa, M. Hirahara, and T. Mukai (1998), Quantification of tailward cold O+ beams in the lobe/mantle regions with Geotail data: Constraints on polar O+ outflows, *J. Geophys. Res.*, *103*(A12), 29,371–29,381.

Shay, M. A., and M. Swisdak (2004), Three-species collisionless reconnection: Effect of O^+ on magnetotail reconnection, *Phys. Rev. Lett.*, *93*, 175,001, doi:10.1103/PhysRevLett.93.175001.

Shelley, E. G., R. G. Johnson, and R. D. Sharp (1972), Satellite observations of energetic heavy ions during a geomagnetic storm, *J. Geophys. Res.*, *77*, 6104–6110, doi:10.1029/JA077i031p06104.

Stepanova, M., V. Pinto, J. A. Valdivia, and E. E. Antonova (2011), Spatial distribution of the eddy diffusion coefficients in the plasma sheet during quiet time and substorms from THEMIS satellite data, *J. Geophys. Res.*, *116*, A00I24, doi:10.1029/2010JA015887.

Toffoletto, F., S. Sazykin, R. Spiro, and R. Wolf (2003), Inner magnetospheric modeling with the Rice Convection Model, *Space Sci. Rev.*, *107*, 175–196, doi:10.1023/A:1025532008047.

Tóth, G., et al. (2005), Space Weather Modeling Framework: A new tool for the space science community, *J. Geophys. Res.*, *110*, A12226, doi:10.1029/2005JA011126.

Tóth, G., D. L. De Zeeuw, T. I. Gombosi, and K. G. Powell (2006), A parallel explicit/implicit time stepping scheme on block-adaptive grids, *J. Comput. Phys.*, *217*, 722–758, doi:10.1016/j.jcp.2006.01.029.

Tóth, G., D. L. De Zeeuw, T. I. Gombosi, W. B. Manchester, A. J. Ridley, I. V. Sokolov, and I. I. Roussev (2007), Sun-to-thermosphere simulation of the 28–30 October 2003 storm with the Space Weather Modeling Framework, *Space Weather*, *5*, S06003, doi:10.1029/2006SW000272.

Tóth, G., et al. (2012), Adaptive numerical algorithms in space weather modeling, *J. Comput. Phys.*, *231*, 870–903, doi:10.1016/j.jcp.2011.02.006.

Waite, J. H., Jr., T. Nagai, J. F. E. Johnson, C. R. Chappell, J. L. Burch, T. L. Killeen, P. B. Hays, G. R. Carignan, W. K. Peterson, and E. G. Shelley (1985), Escape of suprathermal O(+) ions in the polar cap, *J. Geophys. Res.*, *90*, 1619–1630, doi:10.1029/JA090iA02p01619.

Wang, C. P., L. R. Lyons, and T. Nagai (2010), Evolution of plasma sheet particle content under different interplanetary magnetic field conditions, *J. Geophys. Res.*, *115*, A06210, doi:10.1029/2009JA015028.

Welling, D. T., and M. W. Liemohn (2014), Outflow in global magnetohydrodynamics as a function of a passive inner boundary source, *J. Geophys. Res. Space Physics*, *119*, 2691–2705.

Welling, D. T., V. K. Jordanova, S. G. Zaharia, A. Glocer, and G. Toth (2011), The effects of dynamic ionospheric outflow on the ring current, *J. Geophys. Res.*, *116*, A00J19, doi:10.1029/2010JA015642.

Wiltberger, M., W. Lotko, J. G. Lyon, P. Damiano, and V. Merkin (2010), Influence of cusp O^+ outflow on magnetotail dynamics in a multifluid MHD model of the magnetosphere, *J. Geophys. Res.*, *115*, A00J05, doi:10.1029/2010JA015579.

Winglee, R. M., D. Chua, M. Brittnacher, G. K. Parks, and G. Lu (2002), Global impact of ionospheric outflows on the dynamics of the magnetosphere and cross-polar cap potential, *J. Geophys. Res.*, *107*(A9), 1237, doi:10.1029/2001JA000214.

Winglee, R. M., W. K. Peterson, A. W. Yau, E. Harnett, and A. Stickle (2008), Model/data comparisons of ionospheric outflow as a function of invariant latitude and magnetic local time, *J. Geophys. Res.*, *113*, A06220, doi:10.1029/2007JA012817.

Yu, Y., and A. J. Ridley (2009), Response of the magnetosphere-ionosphere system to a sudden southward turning of interplanetary magnetic field, *J. Geophys. Res.*, *114*, A03216, doi:10.1029/2008JA013292.

Zhang, J., et al. (2007), Solar and interplanetary sources of major geomagnetic storms during 1996–2005, *J. Geophys. Res.*, *112*, A10102, doi:10.1029/2007JA012321.